Design Concept of Hybrid Instrument for Laparoscopic Surgery and Its Verification Using Scale Model Test

Yoon-Ho Kim, Yong-Jai Park, *Member, IEEE*, HyunKi In, *Student Member, IEEE*, Chang Wook Jeong, and Kyu-Jin Cho, *Member, IEEE*

***Abstract*—This paper proposes a new design concept of hybrid instrument for single-port laparoscopic surgery (SPLS) and a new method of verification using a scaled-up prototype based on the principle of elastic similarity. The proposed concept is a hand-held instrument that uses a tendon-gear mechanism for dexterous movement of its end-effector and servomotors with flexible tendon-sheath transmission to maintain the dexterity by compensating the loss of output angle from tendon elongation during the manual operation. The kinematic relationship of the tendon-gear mechanism was derived mathematically, and the ratio of external moment to resistive flexural stiffness of the articulating joint was matched between the real-sized model and the large-scale prototype. Our scale model tests have shown good agreement between their input–output relationships under the equivalent loading conditions, and thus verified the validity of similarity analysis. Also, the proof-of-concept experiments have demonstrated the functionality of output loss compensation of the hybrid instrument. Our methodology can be used to simplify and speed up the prototype development process for SPLS by avoiding miniaturization challenges such as high precision manufacturing, which is costly and time-consuming.**

***Index Terms*—Elastic similarity, hybrid laparoscopic surgical instrument, minimally invasive surgery (MIS), scale model test, single-port laparoscopic surgery (SPLS), tendon-gear mechanism.**

I. Introduction

SINGLE-PORT laparoscopic surgery (SPLS), as one of the recently developed techniques in minimally invasive surgery (MIS), has several advantages over traditional open surgery such as small incision, less postoperative pain, and reduced hospital stay [1]. Since SPLS uses only one entry port, typically through the patient's navel, it corresponds more to the ultimate goal of MIS than the multiport laparoscopic surgery and thus is part of the natural development of MIS. Even though the manual control of laparoscopic tools through the single incision point is unnatural and physically demanding for the surgeon, the refinement of instrumentation has resulted in a substantial increase in the use of SPLS in urology over the past few years [2], [3].

In order to avoid collision between the instruments resulting from the confined access, often called *sword fighting*, the hand-held instrument has been developed to have extra degrees of freedom (DOFs) by adopting an articulation for manipulating the end-effector, which is actuated by the antagonistic pair of tendon-like wires. Unlike the conventional instrument that has only five DOFs, the articulated instruments have two more DOFs (pitch and yaw) as shown in Fig. 1. These two additional DOFs enhance the dexterity of operation by providing the surgeon with more wrist-like movement of the end-effector at the surgical site. Various new mechanisms of articulation for improving the dexterity are being invented to be applied to the laparoscopic instruments which have a long and thin stem. However, due to

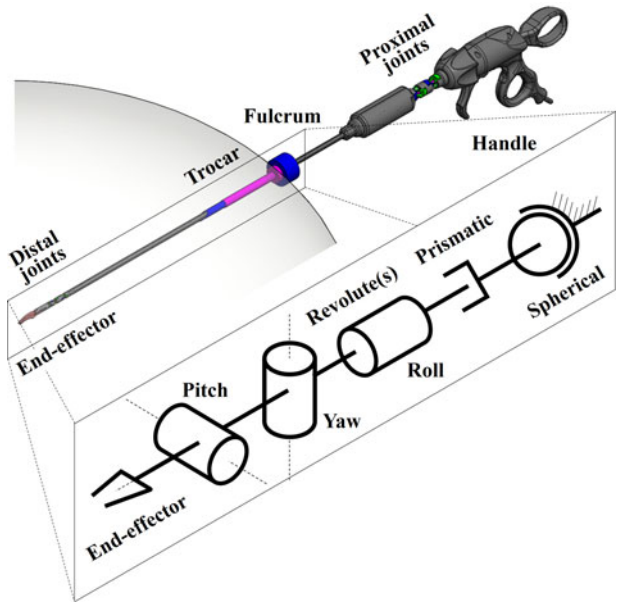

Fig. 1. Mechanical analogy of the hand-held articulated instrument for laparoscopic surgery to the 7-DOF open chain that consists of a spherical joint, a prismatic joint, and a series of three revolute joints. In terms of the end-effector motion, they are kinematically equivalent to each other.

Manuscript received December 1, 2014; revised April 5, 2015; accepted July 2, 2015. Date of publication July 8, 2015; date of current version February 12, 2016. Recommended by Technical Editor S. Q. Xie. This work was supported by a grant (NRCRT-EX15001) of the Translational Research Center for Rehabilitation Robots, Korea National Rehabilitation Center, Ministry of Health & Welfare, Korea.

Y.-H. Kim, H.K. In, and K.-J. Cho are with the BioRobotics Laboratory, School of Mechanical and Aerospace Engineering/IAMD, Seoul National University, Seoul 151-742, Korea (e-mail: kim409@snu.ac.kr; inhk8357@naver.com; kjcho@snu.ac.kr).

Y.-J. Park is with the Robot and Mechanism Laboratory, Department of Mechanical Engineering, Sun Moon University, Asan 336-708, Korea (e-mail: yjpark@sunmoon.ac.kr).

C. W. Jeong is with the Department of Urology, Seoul National University Hospital, Seoul 110-744, Korea (e-mail: drboss@snuh.org).

Color versions of one or more of the figures in this paper are available online at http://ieeexplore.ieee.org.

Digital Object Identifier 10.1109/TMECH.2015.2453321

the small size of the stem whose diameter is only 5 mm, the whole prototype development process is being delayed by the difficulties of actual-size prototyping.

The problems associated with the miniaturization can refer to either high precision machining or obtaining suppliers for the miniature special parts such as gears or pulleys, etc. Both are often too costly and time-consuming to be used to just build the proof-of-concept prototype. For these reasons, a scale-up version of the proposed design has been developed first using the standard parts that are already available off the shelf, while avoiding the problems of miniaturization [4]. The large-scale prototype can be also useful for the performance test of the real-sized instrument, only if some requirements on the similarity are satisfied, given that the experimental setups for its evaluation is quite complicated due to the small size. Indeed, there are virtually no such tiny sensors that are compatible with the confined space of the articulated joints in the market, which would give some information about the angular displacement of the joints or the tendon tension if they were available.

In this paper, we propose a new design concept of the hybrid instrument for SPLS and a new method of its verification and evaluation using a scaled-up prototype based on the similarity analysis. First, we present the mathematical modeling of a tendon-gear mechanism, which is used in the joints of the hybrid instrument to accommodate additional DOFs, and we also present the kinematic relationship between input and output angles which depends on the external loading condition. Then, from the relationship, the loss of dexterity in the movement of the end-effector resulting from the external force is derived quantitatively. Our analytical findings are then supported by the experiments using a scaled-up prototype that we built based on the principle of *elastic similarity*, which is kinematically similar but geometrically dissimilar to the real-sized one for some practical reasons such as convenience of handling in the experiment. We present a methodology for adjusting the elastic similarity which guarantees equivalent input–output relationships for the different-sized models, even when they are geometrically dissimilar or subjected to the external forces of different scales. Compensating performance of the hybrid instrument against the disturbance of external force is also evaluated through the experiment using the large-scale prototype.

II. Hybrid Instrument for Laparoscopic Surgery

One of the biggest challenges that the tendon-driven articulated instrument faces is that the angle of the end-effector decreases when an external force is applied on it. This decrease resulting from the elongation of the tendon is large enough to be recognized by the surgeon during operation, and thus hinders the surgeon from overcoming the tradeoff between operative time and accuracy [5], [6]. This loss of dexterity, inherent to the compliance of the tendon, may be reduced from optimization of the design parameters using the results of theoretical analysis. However, due to the very limited space inside the instrument, it would make no significant changes. Therefore, active compensation of the output loss using motorized actuation is required to enhance the dexterity of operation and consistency of the input–output relationship against the external disturbance.

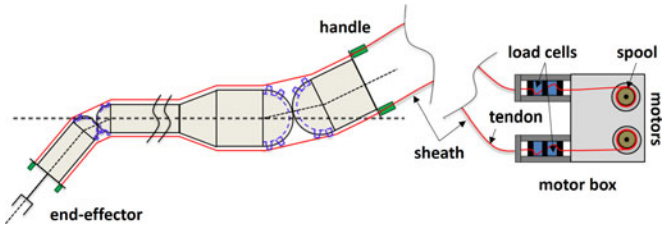

Fig. 2. Schematic representation of the hybrid instrument adopting the tendon-gear mechanism and flexible tendon-sheath transmission system. Each tendon is pulled by a servomotor, and its tension is measured by a load cell equipped in the motor box at the base.

A. State-of-the-Art in Laparoscopic Instrumentation

The most developed instrumentation for laparoscopic surgery at present is teleoperated surgical system such as da Vinci, which is featured by increased accuracy and precision in the multiport surgery [7], [8]. Despite the purported advantages, however, its use in the single-port surgery has been limited to relatively few operations due to its major drawbacks such as spatial limitations, long setup times, high cost, and absence of force feedback [9]. It has been known that the basic laparoscopic task performance is generally faster and as precise using hand-held instruments compared to the robotic systems [10], [11], and clinical efficacy and safety of the robot-assisted surgery over laparoscopic procedures has not been ascertained [12]. All these factors are making the hand-held articulated instruments still highly recommended for SPLS.

Many research works also have presented several designs for the hand-held mechatronic instrument, which is divided into two categories depending on its motor location: one with an end-effector actuated by the motors embedded in the handle [13]–[16], and the other with the motors at a distance from the instrument [17]. The former type is heavy in general and thus ergonomically poor to be applied in the clinical use. The latter one uses the motors fixed at the base while adopting flexible tendon-sheath transmission [18], which allows the end-effector to be manipulated independently of the motor position. This device, however, uses a joystick for manipulation, which is far less intuitive to control than the manual instruments [19].

B. Concept of Hybrid Instrument for SPLS

A hybrid instrument for SPLS is basically same as the conventional articulated instruments in terms of the manual operation by the surgeon. The only difference is the way the surgeon reacts to the output loss. For the conventional instruments, the loss should be compensated manually by increasing the input angle until the end-effector is positioned at the desired angle. However, for the hybrid instrument, the compensation is performed by two servomotors that support precise angling of the end-effector in response to the external loading condition, where the antagonistic pair of tendons is attached through the sheaths (see Fig. 2).

The hybrid instrument is also similar to other motorized devices in terms of the increased accuracy. However, unlike the mechatronic or robotic device that just assists or replaces the maneuvering force of the surgeon with motorized actuation,

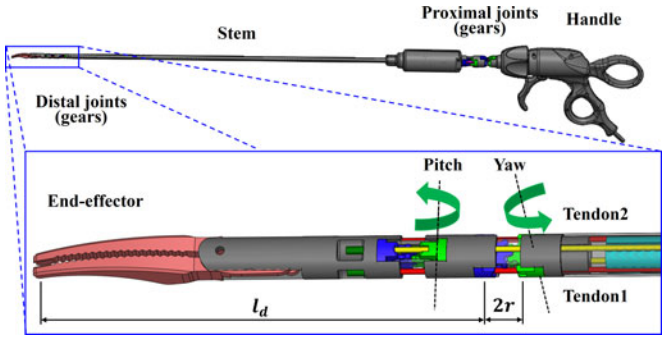

Fig. 3. Detail view of the distal joints of the articulated laparoscopic instrument that has two additional DOFs achieved from the tendon-gear mechanism.

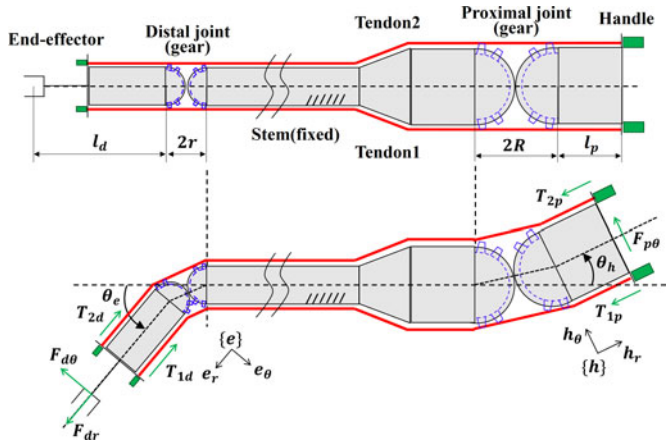

Fig. 4. 1-DOF (in yaw direction) modeling of tendon-gear mechanism for laparoscopic surgical instrument. $F_{d\theta}$ and F_{dr} denote the tangential and the radial forces on the end-effector, respectively, and $F_{p\theta}$ indicates the surgeon's input force on the handle.

the hybrid instrument is basically manipulated by hand and assisted by motors only when there exists an external force. Availability of the comanipulation also makes it distinguished from the purely mechatronic devices, whose motorized assistance and manual operation are decoupled from each other. This is one of the advantages of hybrid instrument, other than the improved accuracy, given that the mechatronic devices have no force feedback as in the case of teleoperated robotic systems [20].

III. Tendon-Gear Mechanism

Tendon-gear mechanism is a patented design for articulation of the tendon-driven laparoscopic instrument, which allows the end-effector to have two more DOFs (pitch and yaw) than that of the conventional 5-DOF instruments [21]. Fig. 3 shows the CAD model of articulated instrument that uses the tendon-gear mechanism. Each joint consists of a pair of interlocking gears, and each gear has two tunnel-like tendon sheaths, each of which contains one of the two tendons at both sides.

When the handle of the instrument is angled, the proximal joint flexes as the teeth of the proximal gears mesh with each other. This locally stretches one of the tendons at the proximal joint, while locally slackening the other side as shown in Fig. 4; however, the entire length of each tendon undergoes no actual change unless an external load is applied to the end-effector. Therefore, the torque generated from the angulation of proximal joint is transmitted to the distal joint through the tendons, which makes the end-effector also rotate in the same direction. The angular deviation of the end-effector is greater than that of the handle, because the distal gears have smaller radii than the proximal ones. However, the fraction of their angular motions is not the gear ratio, unlike our expectation at a glance, which we will see in the remaining sections of this paper.

A. Theoretical Modeling of Tendon-Gear Mechanism

Understanding transmission characteristics of the tendon-gear mechanism is essential for the model-based approach. In general laparoscopic surgery, dynamic behavior of the end-effector such as angular velocity or acceleration is not required; instead, kinematic relationship between input and output angular displacement and the torque transmission characteristics are more important. Therefore, in this paper, the input–output relationships for angular displacement and torque are derived under the assumption of *quasi-static equilibrium* in the presence of an external force applied to the end-effector.

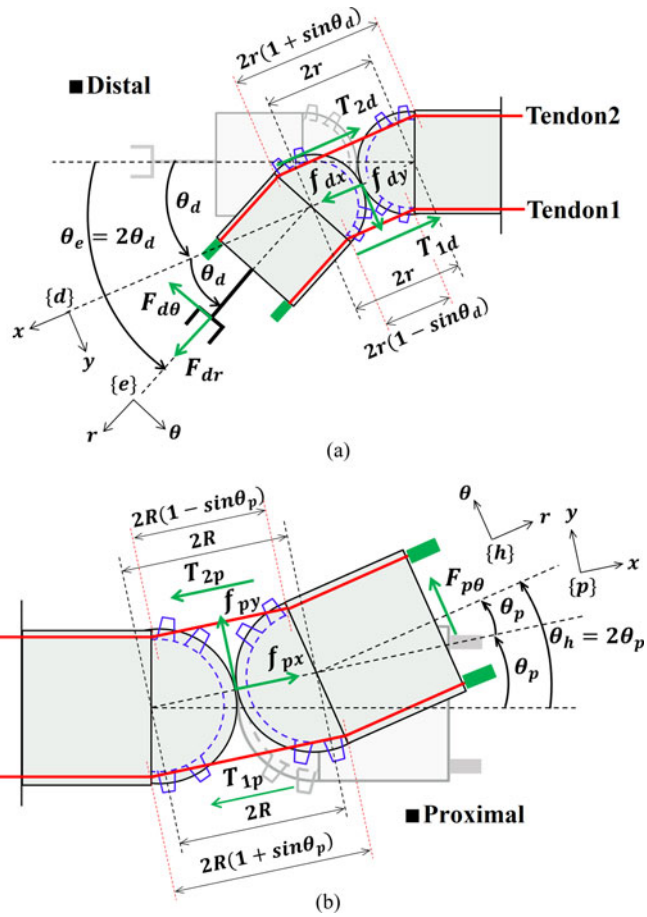

Fig. 5. Free body diagrams of (a) distal joint and (b) proximal joint.

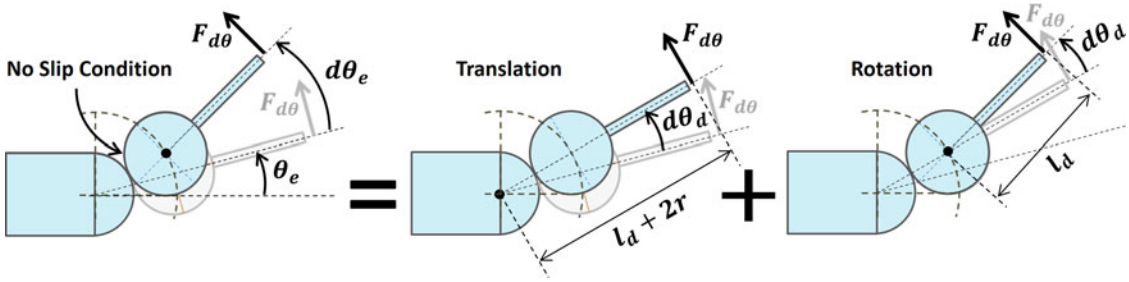

Fig. 6. Decomposition of the end-effector motion into curvilinear translation and rotation.

Since pitch and yaw movements of the end-effector are independent of each other for the tendon-gear mechanism, meaning that the resultant 2-DOF motion can be analyzed merely by integrating the two separate results for 1-DOF motions, a simplified planar model was used for theoretical modeling of the tendon-gear mechanism as depicted in Fig. 4. It is worth noting that the end-effector actually has five more DOFs: four at the fulcrum, or pivot point, which are equivalent to a combination of the ball joint and the prismatic joint; and the other one at the revolute joint for rolling motion (see Fig. 1).

Free body diagrams of the distal and proximal joints are presented in Fig. 5 with all the forces being applied: reaction forces between meshed teeth of the distal and proximal gears $(f_{dx}, f_{dy}, f_{px}, f_{py})$ tendon tensions at each joint $(T_{1d}, T_{1p}, T_{2d}, T_{2p})$ and external forces on the end-effector $(F_{d\theta}, F_{dr})$ and handle $(F_{d\theta})$. Because the joint motion can be decomposed into curvilinear translation and rotation around the center of the moving gear, as depicted in Fig. 6, two reference frames are required for each joint to describe all the forces in Fig. 5.

Equations for moment equilibrium about the contact points of the interlocking gears at the distal (1) and the proximal joints (2) are derived as follows:

$$T_{1d} - T_{2d} = F_{d\theta}\left(\frac{l_d}{r\cos\theta_d} + 1\right) - F_{dr}\sin\theta_d \tag{1}$$

$$T_{1p} - T_{2p} = F_{p\theta}\left(\frac{l_p}{R\cos\theta_p} + 1\right). \tag{2}$$

If we assume that the only factor that makes disparity between distal and proximal tensions is the friction between tendon and sheath, and also assume that is negligible, the tendon tension would be uniformly distributed over the entire length, that is:

$$T_{id} = T_{ip}, \quad i = 1, 2. \tag{3}$$

For convenience, let the subscripts 1 and 2 denote the agonist and antagonist tendons, respectively. When the joints are flexed in the presence of external forces as shown in Fig. 5, the change in length of the agonist tendon becomes

$$\delta_1 = 2\left(R\sin\theta_p - r\sin\theta_d\right) \tag{4}$$

while that of the antagonist becomes

$$\delta_2 = 2\left(r\sin\theta_d - R\sin\theta_p\right). \tag{5}$$

Given that the tendon is elastic where the passive tension can develop, the variations of tendon tensions are calculated as

$$T_1 - T_o = 2k\left(R\sin\theta_p - r\sin\theta_d\right) \tag{6}$$

$$T_2 - T_o = 2k\left(r\sin\theta_d - R\sin\theta_p\right) \tag{7}$$

where k denotes the tendon stiffness, and T_o the initial tension. If the amount of tension variation in the antagonist tendon exceeds the initial tension, the antagonist would slack to have no more tension. Thus, the difference of tendon tensions $(T_1 - T_2)$ should be expressed separately, before and after the slack occurs, as (8). Note, however, that the separate expression does not necessarily mean there appears a discontinuity

$$T_1 - T_2 = \left\{\begin{array}{l} 4k\left(R\sin\theta_p - r\sin\theta_d\right)\left(T_o > |\Delta T|\right) \\ T_o + 2k\left(R\sin\theta_p - r\sin\theta_d\right)\left(T_o \le |\Delta T|\right) \end{array}\right\}. \tag{8}$$

From (1), (3), and (8), we can derive an equation that relates the angular displacements with the external forces as follows:

$$\sin\theta_d = \left\{\begin{array}{ll} \frac{R}{r}\sin\theta_p - \frac{F_{d\theta}}{4kr}\left(\frac{l_d}{r\cos\theta_d} + 1\right) & \left(T_o > |\Delta T|\right) \\ \frac{R}{r}\sin\theta_p - \frac{\left(F_{d\theta}\left(\frac{l_d}{r\cos\theta_d}+1\right) - T_o\right)}{2kr} & \left(T_o \le |\Delta T|\right) \end{array}\right\}. \tag{9}$$

External force on the end-effector can be divided into tangential and radial components, but only the tangential force is included in (9) while the radial force is neglected. This is because tasks in general procedures of the laparoscopic surgery such as suturing require relatively less force in radial direction than the tangential one. Moreover, the radial force cannot contribute enough to the external moment on the end-effector, because it has much shorter moment arm about the point of contact between the gear pitch circles than that the tangential force has (see Fig. 5(a)). Finally, most of the radial force is supported and thus canceled out by the links connecting the two gears at the distal joint, whereas the tangential force can only be supported by the difference between the tendon tensions at both sides.

B. Force-Dependent Input–Output Relationship

The input–output relationship represented by (9) is plotted in Fig. 7. The dashed line indicates the linear relationship $\theta_e = (R/r)\theta_h$ determined by the gear ratio, which we are prone to expect when it comes to the geared transmission. However, the

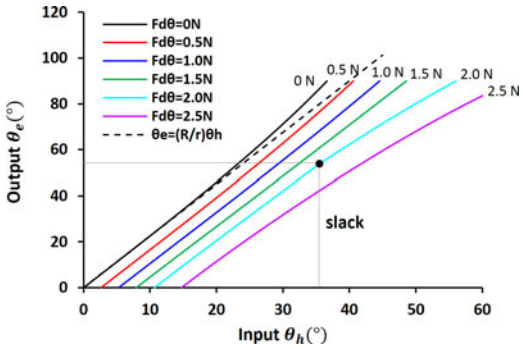

Fig. 7. Input–output relationship of the tendon-gear mechanism derived from mathematical modeling, where all of the system parameters and external loading conditions are determined based on the real-sized instrument. Initial tension T_o was presumed as 30 N.

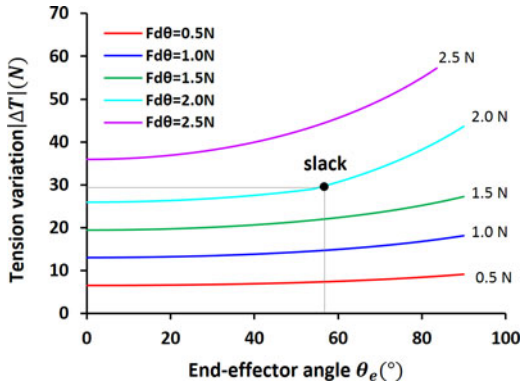

Fig. 8. Variation of tendon tension resulting from configuration change of the tendon-gear mechanism, which was derived from the mathematical modeling under several loading conditions. Since the initial tension T_o was set to be 30 N, slack in the antagonist tendon occurs when the tension variation reaches 30 N.

mathematical modeling revealed the nonlinear characteristic of the tendon-gear mechanism as shown in the figure.

Both of the tendons should be pretensioned to transmit the torque, and magnitude of the initial tension determines whether the slack occurs under a certain amount of external force on the end-effector. Where the slack occurs and how it affects the transmission characteristics can be observed at the concave-to-convex transition point. As shown in Fig. 7, the input–output curve is slightly concave upward because of the inherent nonlinearity, but it becomes convex upward after the slack occurs.

This concave-to-convex transition resulting from the slack can be physically understood. Before the slack occurs, while the tangential force $F_{d\theta}$ is being applied on the end-effector in direction that impedes the flexion of distal joint, the increase of agonist's tension and the decrease of antagonist's tension make positive moments of equal amount that resist the negative external moment. However, once the antagonist tendon slacks, only the agonist can make the resistive moment. Therefore, the angle of the end-effector becomes relatively lower than it would be if there occurred no slack.

Tension variations in agonist and antagonist tendons are in equal amount, but only their signs differ from each other; one increases while the other one decreases. The variation of tendon tension corresponding to the end-effector's angular position is presented in Fig. 8, which was simply derived by substituting the input–output relationship (9) under several loading conditions into (6) or (7). Profiles of tendon tensions against the angular state of the end-effector can be predicted from this figure.

C. Torque Transmissibility

Torque transmission characteristic of the tendon-gear mechanism, as well as the kinematic relationship, is also important for high dexterity and maneuverability of the instrument. Thus, the *torque transmissibility* (ξ), defined as a ratio of the input and output moments, was derived by calculating the external moment at each joint generated from the tangential force applied on the end-effector or handle.

Assume that an input tangential force $F_{p\theta}$ on the handle is transmitted to the end-effector and makes $F_{d\theta}$ as an output force on it. Since the angular motion of the end-effector can be divided into curvilinear translation and rotation, as mentioned earlier, the output moment can be derived simply by summing the corresponding two components calculated separately:

$$M_o = \frac{dW_{\text{out}}}{d\theta_d} = F_{d\theta}\left(l_d + 2r\right) + F_{d\theta} l_d. \tag{10}$$

Likewise, the input moment can be derived as follows:

$$M_i = \frac{dW_{\text{in}}}{d\theta_p} = F_{p\theta}\left(l_p + 2R\right) + F_{p\theta} l_p. \tag{11}$$

Then, the torque transmissibility can be expressed as

$$\xi = \frac{M_o}{M_i} = \frac{F_{d\theta}\left(l_d + r\right)}{F_{p\theta}\left(l_p + R\right)}. \tag{12}$$

Then, we can rewrite (12) by using (1)–(3) to replace $F_{d\theta}/F_{p\theta}$ with another expression that only contains the system parameters (l_d, l_p, r, R) and the input–output variables (θ_p, θ_d):

$$\xi = \left(\frac{r\cos\theta_d}{R\cos\theta_p}\right)\left(\frac{l_p + R\cos\theta_p}{l_d + r\cos\theta_d}\right)\left(\frac{l_d + r}{l_p + R}\right). \tag{13}$$

Given that the laparoscopic surgical instrument is so slender that $l_p \gg R$ and $l_d \gg r$, (13) can be reduced to a simpler form:

$$\xi = \frac{r\cos\theta_d}{R\cos\theta_p}. \tag{14}$$

The torque transmissibility under several loading conditions is presented in Fig. 9. As expected from (14), the torque transmissibility depends on both the configuration change of the instrument and the external force. However, unlike the input–output relationship or tendon tension variation, the effect of the external loading is much weaker. Reduction of the torque transmissibility resulting from the increase of end-effector angle can be physically explained by observing the change of moment arm. The moment arm of the tendon tensions at the distal joint is $r\cos\theta_d$, while that at the proximal joint is $R\cos\theta_p$. Both of them decrease as θ_d and θ_p increase during the flexion of each joint, but the overall ratio should decrease as θ_d increases faster than θ_p does.

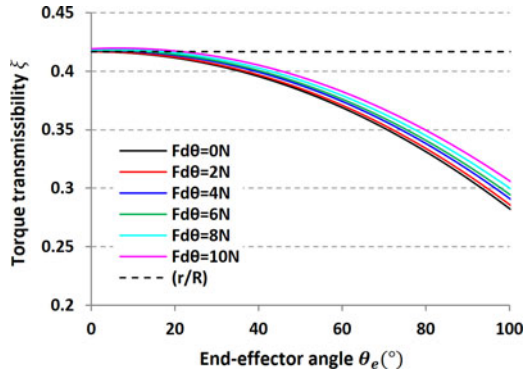

Fig. 9. Torque transmissibility plotted against the end-effector angle and its variation depending on the external force applied on the end-effector.

IV. Similarity Analysis

A. Principle of Elastic Similarity

In this paper, the similarity issue was focused on whether the different-sized models have a quasi-statically identical input–output relationship under the equivalent external loading condition, which is closely related to the inherent compliance of joints of the tendon-driven instrument. Therefore, this aspect of design principle should be referred to as *elastic similarity*. By defining a relationship between a flexural stiffness of the distal joint and an external moment exerting on it, we formulate the required condition for ensuring the elastic similarity between the models of different scales.

In general scale model test, the geometric similarity is often considered as a primary condition that has to be met first, followed by the kinematic and dynamic similarities. However, it is not always possible to achieve strict similitude between the different-sized models. For example, in this study, implementing a magnetic encoder at the distal joint, which is necessary for evaluating the performance of the prototype, requires the model to be at least threefold larger than the real-sized one. However, since the instrument is so slender due to its long and thin shaft, the overall length would be almost human height if its size were just increased threefold, which would be quite awkward to operate manually. Therefore, in this study, the geometric similarity was intentionally ignored for convenience, and the geometric parameters were adjusted to have their own scaling factors, which may differ from each other.

It is worth noting that the elastic similarity is not necessarily preceded by the geometric similarity; the scaled-up prototype can satisfy the elastic similarity even if its geometry is no longer similar to the model's one. This must not be confused with elastic similarity in the literatures [22]–[24], one of the biological scaling laws for different-sized animals to preserve similar resistance to column buckling from their weights [25], [26], which is only applicable between geometrically similar entities. Thus, what we suggest in this paper is more general and broader concept of the elastic similarity than that in the biology, even though they can be understood in the same context as the similitude related to the elastic deformation.

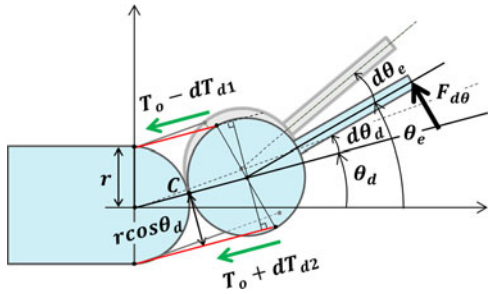

Fig. 10. Additional flexion of distal joint due to the external force tangentially exerting on the end-effector. Tension of the agonist tendon decreases by dT_{d1}, and that of the antagonist tendon increases by dT_{d2}, both from the same initial tension T_o.

Fig. 10 depicts the distal joint and the end-effector subjected to the tangential force $F_{d\theta}$. Imagine you are holding the handle at an input angle θ_h and thus the end-effector is indicating the corresponding output angle θ_e. Next, suppose an external force $F_{d\theta}$ is applied tangentially at the end tip of the instrument, as shown in the figure, while the input angle θ_h you are holding remains unchanged. Then, the tendon compliance would allow the distal joint to flex more by $d\theta_d$, though there is no displacement of the tendon's proximal end tip driven by the angulation of the proximal joint. During this additional flexion, the end-effector would deviate twice greater because of the resultant motion of curvilinear translation and rotation $(d\theta_e = 2d\theta_d)$. Variation of each tendon tension during this additional flexion makes a resistive moment (M_{resist}) against the external force, whose derivative with respect to θ_d would be approximated as

$$\frac{dM_{\text{resist}}}{d\theta_d} \approx r\cos\theta_d \times \left(\frac{dT_2}{d\theta_d} - \frac{dT_1}{d\theta_d}\right). \tag{15}$$

Then, by replacing $dT_1/d\theta_d$ with $-2kr\cos\theta_d$ and $dT_2/d\theta_d$ with $2kr\cos\theta_d$, respectively, and using θ_e instead of θ_d, we could get an expression for a *2-D resistive flexural stiffness* κ_θ as follows:

$$\kappa_\theta = \frac{dM_{\text{resist}}}{d\theta_e} = 2kr^2\cos^2\left(\frac{\theta_e}{2}\right). \tag{16}$$

Unlike the 3-D beam, as its dimension implies, the distal joint's bending occurs only on a plane that is determined by the two tendons, whose diameters are negligible. Therefore, strictly speaking, κ_θ should be referred to as 2-D resistive flexural stiffness; however, for the sake of convenience, we would just use the *resistive flexural stiffness* in the rest of this paper.

Now we can define the *loss of dexterity* (Θ) mathematically, as a ratio of external moment to the resistive flexural stiffness:

$$\Theta = \frac{M_{\text{ext}}}{\kappa_\theta} = \frac{F_{d\theta}\,(l_d + r\cos(\theta_e/2))}{2kr^2\cos^2(\theta_e/2)}. \tag{17}$$

Physical implication of this parameter can be additional flexion or loss of output angle of the end-effector, depending on the direction of the external force. Equivalent loss of dexterity (Θ) between the different-sized models of tendon-driven instrument is a necessary condition for elastic similarity that assures the same force-dependent input–output relationship.

TABLE I
DESIGN PARAMETERS OF MODEL AND PROTOTYPE

Parameter	Description	Model	Prototype	Scale
$\emptyset$ (mm)	Stem diameter	5	18.75	3.75
L (mm)	Overall length	500	1000	2
r (mm)	Radius of distal gear	2	7.5	3.75
R (mm)	Radius of proximal gear	4.5	16.875	3.75
l_d (mm)	See Fig. 4	50	86	1.72
l_p (mm)	See Fig. 4	120	160	1.33
d (mm)	Tendon diameter	0.63	0.54	0.857
E (GPa)	Young's modulus	50	50	1
k (N/m)	Tendon stiffness	31 172	11 451	0.367

TABLE II
SCALE FACTORS FOR VARIABLES

Variable	Description	Scale
$F_{d\theta}(N)$	External force	2.88
$T(N)$	Tendon tension	1.377
Θ	Loss of dexterity	1

The principle of elastic similarity can also be applied to other types of tendon-driven mechanisms, even though its mathematical expression may differ from each other. For example, the tendon-pulley mechanism has $2kr^2\theta_e$ for its resistive torsional stiffness [27], [28], whereas the tendon-driven continuum manipulator [29], [30] that contains a flexible beam would require more complicated expression for its 3-D resistive flexural stiffness. The expression of external moment (M_{ext}) would also depend on the type of tendon-driven mechanisms.

B. Scaling Factors for Design Parameters

Design parameters of the scaled-up prototype and real-sized model, which were derived from the elastic similarity analysis, are listed in Table I. The stem diameter ($\emptyset$) and gear radii (r, R) were scaled up by a factor of 3.75, while the other linear dimensions (L, l_d, l_p) were scaled up individually with different scale factors lower than 3.75. This made the enlarged prototype far less slender than the model, so that it could be much easier to handle during the scale model test. Tendon stiffness (k) of the prototype was about three times lower than that of the model due to the decreased diameter and the increased length of the tendon prototype was about three times lower than that of the model due to the decreased diameter and the increased length of the tendon. After all of the system parameters were determined, the scaling factor of external force ($F_{d\theta}$) was also determined to be 2.88 to make the loss of dexterity (Θ) identical for both prototype and model as shown in Table II.

V. DESIGN OF OUTPUT LOSS COMPENSATION

A. Determination of Compensation Angle

For given input θ_h, the desired output angle θ_e^* is determined from the *reference kinematic relationship*, which is defined as an input–output relationship under no external force on the end-effector (see Fig. 11). The reference kinematic relationship is easily obtained by substituting zero into external force $F_{d\theta}$ in

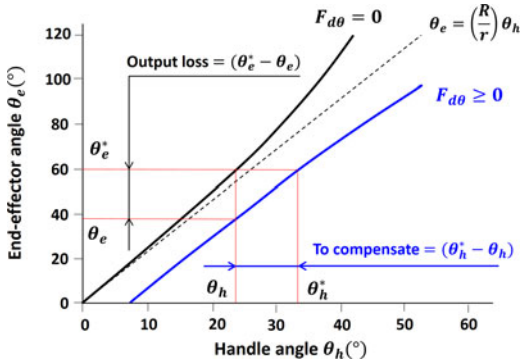

Fig. 11. Model-based estimation on the loss of output angle caused by external force and the amount of input angle to be increased to compensate the output loss.

(9) as follows:

$$\theta_e^* = 2\sin^{-1}\left(\frac{R}{r}\sin\left(\frac{\theta_h}{2}\right)\right). \tag{18}$$

Then, the output angle θ_e in the presence of external force can be obtained as (19) from the model-based estimation presented earlier. Input angle θ_h and tendon tensions T_1, T_2 are measured from a proximal encoder and two force transducers embedded in the instrument, respectively

$$\theta_e = 2\sin^{-1}\left(\frac{R}{r}\sin\left(\frac{\theta_h}{2}\right) - \frac{(T_1 - T_2)}{4kr}\right). \tag{19}$$

Then, the output loss due to the external load becomes $(\theta_e^* - \theta_e)$, and the amount of input angle to be compensated would be $(\theta_h^* - \theta_h)$, as depicted in Fig. 11. If we rewrite (19) in terms of θ_e^* and θ_h^*, we can obtain an expression for the new input θ_h^* required to achieve the desired output θ_e^* under the external force as follows:

$$\theta_h^* = 2\sin^{-1}\left(\frac{r}{R}\sin\left(\frac{\theta_e^*}{2}\right) + \frac{(T_1 - T_2)}{4kR}\right). \tag{20}$$

In order to compensate the output loss $(\theta_e^* - \theta_e)$, on the one hand for conventional instruments, the surgeon should increase the input angle manually by $(\theta_h^* - \theta_h)$. On the other hand for the hybrid instrument, the servomotor on the agonist's side—one with the direct connection to the agonist tendon among the antagonistic pair of motors—can be used to make up the output loss by pulling the agonist tendon by the same amount of its linear displacement corresponding to the angular displacement $(\theta_h^* - \theta_h)$. Then, referring to the tendon 1 depicted in Fig. 5(b), we can determine the amount of linear displacement Δl_{1p} to be compensated as follows:

$$\begin{aligned}\Delta l_{1p} &= 2R\left(1 + \sin\left(\frac{\theta_h^*}{2}\right)\right) - 2R\left(1 + \sin\left(\frac{\theta_h}{2}\right)\right) \\ &= 2R\left(\sin\left(\frac{\theta_h^*}{2}\right) - \sin\left(\frac{\theta_h}{2}\right)\right).\end{aligned} \tag{21}$$

Now, by substituting (18) and (20) into (21), we can obtain an expression for the operation input φ^* that is required for motor

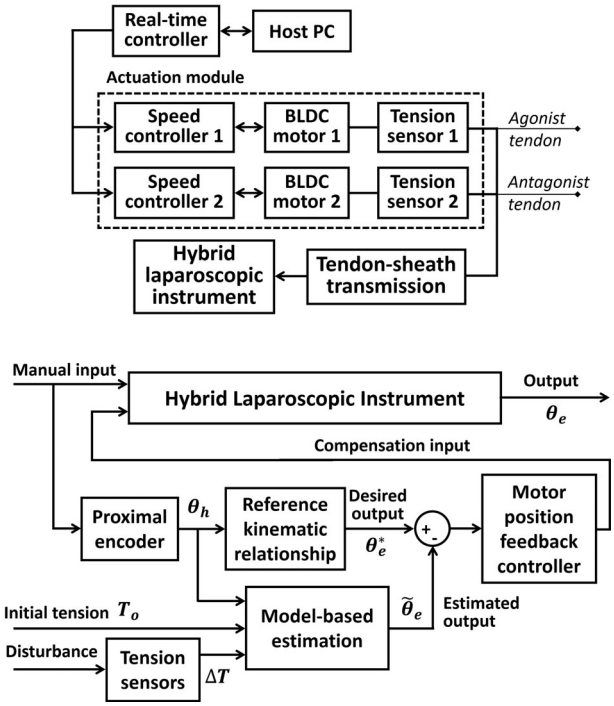

Fig. 12. (a) Schematic representation of a system architecture of the hybrid instrument for SPLS. (b) Feedforward control algorithm for output loss compensation of the prototype of hybrid instrument for SPLS.

to compensate the output loss:

$$\varphi^* = \frac{T_1 - T_2}{2kr_s} \tag{22}$$

where r_s denotes the radius of a spool connected to the motor, and the input angle φ^* is expressed in radian. The difference of tendon tensions can be measured from the force transducers.

B. Feedforward Control for Output Loss Compensation

The hybrid instrument is basically operated by angling the handle manually, while the compensation of output loss against the disturbance such as external force is conducted by means of motorized actuation and its control. The control of actuation, however, has much less options compared to other systems, because the real-sized instrument can hardly be equipped with a distal sensor for measuring the end-effector's angular position. In other words, the output variable cannot be fed back into the adjustment of the motor positions for output loss compensation; instead, the end-effector angle should depend solely on the estimation obtained from the mathematical model.

Fig. 12 shows a block diagram of our feedforward control algorithm for the prototype of hybrid instrument. Angular position of the end-effector, as an output of the whole system, is controlled by the two input signals: the manual operation and the motorized compensation. Disturbance to the end-effector position can be detected by the tension sensors, because the manipulator configuration and the tendon tension are coupled with each other. Disturbance (ΔT), angular position of handle (θ_h) which is achievable from the proximal encoder, and initial tension (T_o) are used to calculate the estimation of output angle $(\tilde{\theta}_e)$. Then, the difference between the desired output (θ_e^*) and the estimated output $(\tilde{\theta}_e)$, or simply the pseudo-error, is used as an input variable for the feedback control of the motor position.

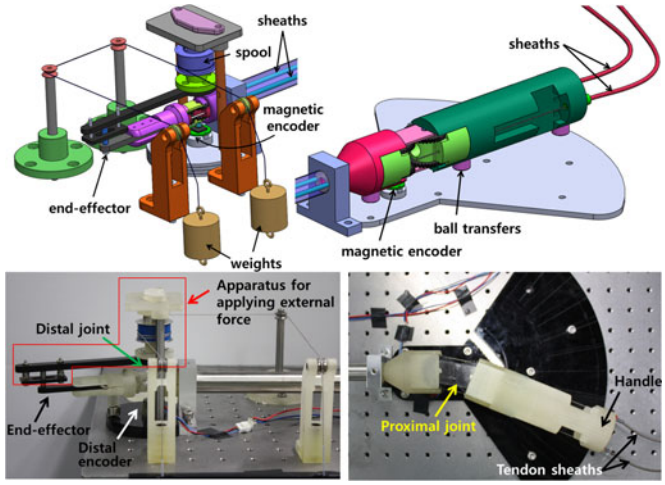

Fig. 13. Experimental design using a scaled-up prototype of the hybrid instrument with a force-applying device.

VI. Experimental Setups

Experimental investigation of this study was designed in two steps: verification of the theoretical modeling of input–output relationship of the tendon-gear mechanism, and assessment of the compensating performance of the designed prototype.

First, to verify the input–output relationship predicted from the modeling, we devised a force-applying device (see Fig. 13) that can generate a constant force always being applied tangentially on the end-effector even when its angular position has been changed. We could generate a constant torque, as much as we intended by adjusting the difference of the weights shown in Fig. 13, which was transmitted to the end-effector through the rigid bar. Since the bar has a slotted link that can slide freely in radial direction, it could transmit only the tangential force to the end-effector as we intended to. For three different tangential forces, we tracked the angular positions of the end-effector and handle varying the amount of angulation of the handle.

Second, we demonstrated the output loss compensation of the prototype to test its characteristics and assess the performance of the compensation against the external disturbance. We applied an external force to the end-effector while activating the compensation control mode, so that the prototype could react automatically to the disturbance. To make a quantitative comparison, we tracked the time response of the output angle until the compensation was completed.

The angular positions of end-effector and handle were measured by means of a magnetic encoder (Renishaw RMB20V) mounted at each joint. And the tendon tension was measured by two force transducers (Ktoyo 333FB) embedded in the instrument as illustrated in Fig. 2. Based on the LabVIEW software installed in a National Instrument CompactRIO (cDAQ-9178), we acquired and processed the analog output from distal and

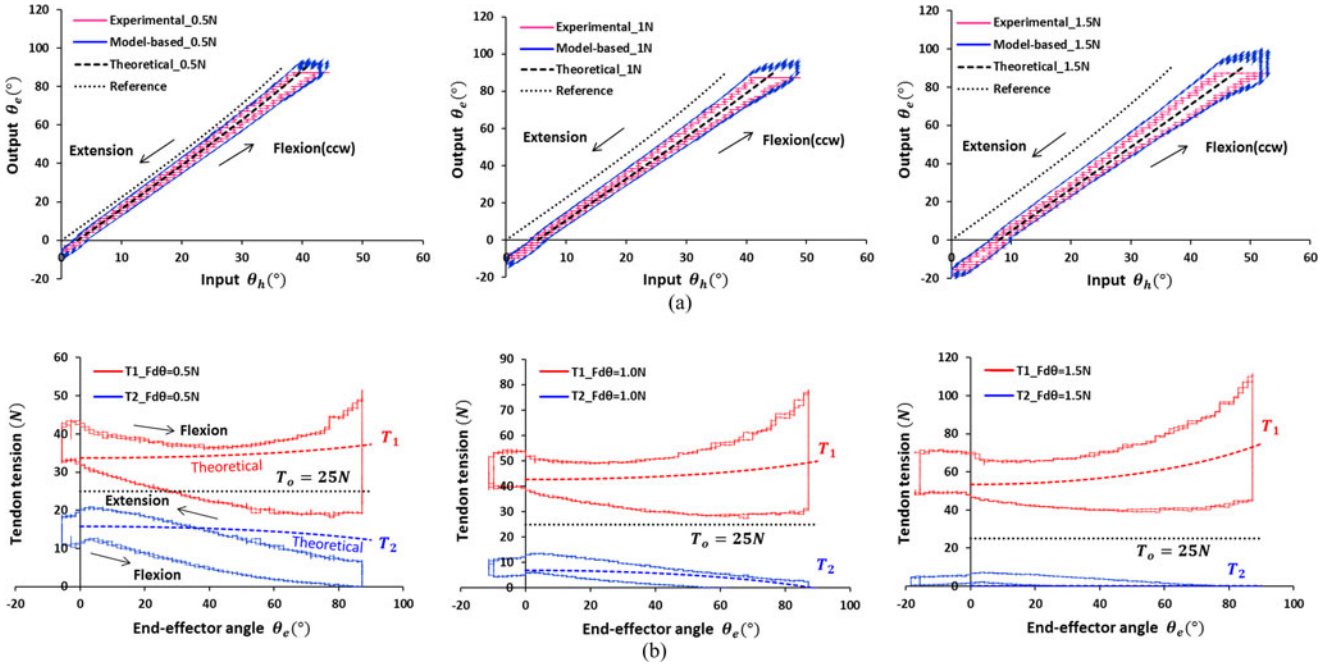

Fig. 14. (a) Input–output relationships corresponding to the applied tangential forces; 0.5, 1.0, and 1.5 N, when the initial tension was 25 N. In each graph, the dashed line represents the result of theoretical modeling, and the dotted line shows the relationship when there is no external force as a reference. The red lines forming a smaller hysteresis loop show the measured values of input and output angles during two consecutive cycles of flexion and extension. Model-based estimation of the output angle using measurements of tendon tensions and input angle is plotted by the blue lines which form a larger hysteresis loop. (b) Tendon tension variations during two consecutive cycles of flexion and extension. The horizontal dotted line in the middle represents the initial tension (T_o), and the red and blue dashed lines above and below the initial tension represent the theoretical values for both tendon tensions achieved from the modeling.

proximal magnetic encoders and two force transducers, where the data were recorded at 2000 samples/s. Two brushless dc motors with speed control drivers (Faulhaber) were used.

VII. Results and Discussion

A. Verification of Theoretical Modeling

Through the mathematical modeling, we presented the anticipated results of the force-dependent characteristics of input–output relationship in Fig. 7. Experimental results have revealed the true characteristics of tendon-gear mechanism, as shown in Fig. 14. Some significant observations are described later.

First, the principle of elastic similarity was proved from the experiment. The results in Fig. 14(a) showed satisfactory agreement between the theoretical prediction marked as the dashed line, which was calculated based on actual dimension of the instrument, and the measurement achieved from the large-scale prototype. This demonstrates that the elastic similitude can be ensured if the *loss of dexterity* (Θ) is identical, even when their geometry is no longer similar to each other.

Second, the effects of friction were demonstrated from the experiment. In Fig. 14(a), the input–output curves from the measurement formed a hysteresis loop, whose bandwidth implies a backlash resulting from the change in direction of the friction at the transition point between flexion and extension. The fact that the rightward shift with respect to the theoretical curve is greater than the leftward shift can be explained from the tendon tension measurements in Fig. 14(b). The agonist's tension T_1 was higher at flexion, while the antagonist's tension T_2 was higher at extension. However, since the overall effects of friction is greater at flexion due to the higher tension, the curve shifts more during flexion than extension.

Third, our model-based estimation showed sufficient accuracy toward the experimental data as shown in Fig. 14(a): the root mean squared error was 2.18°, 2.38°, and 2.97°. Note that the theoretical model, which was a basis of the model-based estimation, neglected the friction term assuming its marginal effect on the tendon tension, though it turned out to be not negligible from Fig. 14(b) presumably due to its concentration on the vertices of tendon at the articulated joints. However, our model-based estimation showed good agreement with the measurement, and this can be logically understood when considering that the effect of friction was already reflected in the tendon tensions (T_1, T_2) measured from the proximal force transducers, which were the input variables in (22) to the model-based estimation as depicted in Fig. 12(b).

B. Evaluation of Compensating Performance

We conducted experiments to assess the compensation performance of the prototype subjected to an external force. Four undisturbed states were chosen as our experimental conditions: input angles (0°, 10°, 20°, and 26°); and the output angles (0°, 33°, 67°, and 80°) as their corresponding counterparts. There was no external force at the beginning of each measurement, but after a few seconds, an external moment of 0.15 N·m started to be applied to the distal joint as a disturbance. The external moment was generated by applying 10-N force at one of the

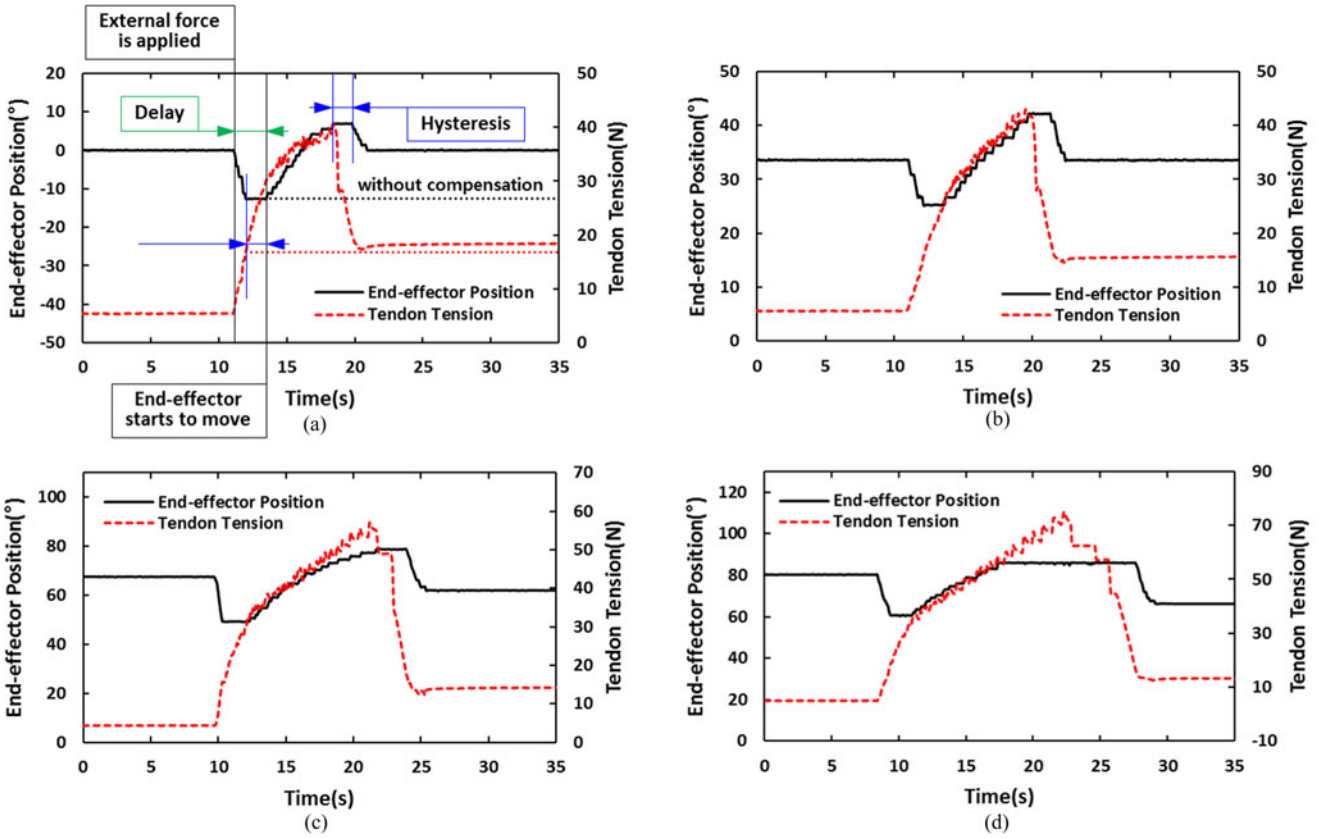

Fig. 15. Time responses of end-effector angle and agonist tendon tension of the hybrid instrument to the external load that was suddenly imposed on the end-effector. In order to investigate how the friction depending on the manipulator configuration affects the compensation performance of the prototype, four different initial conditions for the end-effector angle were set: (a) 0°, (b) 33°, (c) 67°, and (d) 80°. The corresponding initial angles of the handle were (a) 0°, (b) 10°, (c) 20°, and (d) 26°, and the external load applied on the end-effector was 10 N, which is equivalent to 1.5 N for the real-size instrument when taking account of the elastic similarity. (a) Evaluation of compensation performance and analysis of time response of the scaled-up prototype for hybrid instrument. The solid line denotes the angular position of the end-effector that varies with time, and the dashed line indicates the agonist tendon tension that corresponds to the angular position of the end-effector. The dotted lines show what the end-effector position and tendon tension would be if there were no compensation.

weight-holding cables in the force-applying device (see Fig. 13). This 0.15-N·m moment generated a constant force of 1.5 N exerting tangentially on the end-effector. It is worth noting, when taking account of the elastic similarity, that the 1.5-N external force acting on the prototype is equivalent to a 0.52-N force on the end-effector of the real-sized model (see Table II).

Performance of the compensation was assessed by analyzing the time response of output angle against the disturbance at each state as shown in Fig. 15(a). The external force is applied near at 10 s, where the output angle starts to drop quickly to a certain level. As the tendon tension increases, the angular displacement that the motor should compensate is calculated from (22), and the motor starts to pull the tendon by rotating its spool onto which the tendon is wound. At the beginning of the compensation, there occurs a few seconds of time delay between the motions of the motor and the end-effector. During this period of delay, the tendon tension increases as one of its end tips is being pulled by the motor, while the other tip stays stationary. This is because the static friction at distal joint hinders the end-effector from following the motor movement. The friction exists throughout the whole sheath along the tendon path, while most of it is concentrated on the vertices of the tendon (see Fig. 5) at both distal and proximal joints. However, what primarily determines whether the end-effector moves or stays is the friction at the distal joint because the sharper vertex has much greater friction.

After the delay ends, the end-effector begins to move as the static friction acting on the distal vertices reaches its maximum. From this point, the increasing rate of the tension decreases as observed in Fig. 15(a). The reason for this decrease can be explained by two factors: 1) transition from static to kinetic friction at the vertices of distal joint; and 2) movement of the distal end tip of the tendon following the motor's pulling of its proximal end tip. When the end-effector stayed stationary during the period of delay, all amount of the increase in tension contributed to the elongation of tendon. However, when compared to the delay period, the rate of tendon elongation declines now that the end-effector moves in the direction that the motor is pulling its tendon. Note that this decrease in slope of the tension curve did not result from the reduction of revolution speed of the motor. Since the input current that determines the motor speed was kept almost constant, as a result of nonlinear feedback control of the motor position, the output loss compensation was also maintained at a constant rate.

In Fig. 15(a), angular position of the end-effector culminates before being stabilized, which seems like a mild overshoot. The

overshoot, in general, is an indicator of instability that occurs when the control gain is too high. However, that observed in the figure would rather be attributed to the inherent weakness of the feedforward control, combined with the effects of friction. The static friction increased the tendon tension drastically at the beginning of the compensation, which made the motor input and the corresponding output angle of the end-effector exceed the amount actually required for the compensation. Then, at a certain point, the motor started to release the tendon dropping its tension quickly to a certain level that was raised from the initial tension by the external load. Note that this level indicating the net increase of tension due to external force is marked as the dotted lined above the initial tension in Fig. 15(a). After a few seconds of hysteresis, the end-effector started to move in the opposite direction and was stabilized at the desired position.

The results in Fig. 15(a) showed that the prototype used in the experiment had satisfactory performance of the output loss compensation. However, as shown in the others of Fig. 15, not all of the results were satisfactory. The result in Fig. 15(b) was barely tolerable given that the output angle was stabilized at the desired position, despite the larger overshoot compared to that in Fig. 15(a). Meanwhile, those in Fig. 15(c) and (d) showed quite poor performance. This disparity between the experimental results is attributed to the inequality of friction at the four different conditions for the manipulator configuration. That is, as the input and output angles become larger, the vertices of tendons at both joints are sharpened to have greater friction which causes more considerable influence on the performance. For this reason, much larger errors were observed in the experiments with larger joint angles for their initial conditions. However, the initial conditions in Fig. 15(c) and (d) can be regarded as quite close to or almost extreme for manipulator configuration, given that the range of motion of the end-effector is typically ranging from 0° to 80° for the general articulated instruments [2], [5]. Thus, it can be stated that our experimental results and the analytical findings are meaningful for further refinement of the output loss compensation.

VIII. Conclusion

In this paper, we proposed the design concept of the hybrid instrument, which compensates the loss of dexterity with motorized assistance while keeping the manual operation for intuitive control, to enhance the dexterity of operation in the SPLS. Also, we formulated the principle of elastic similarity and applied it to the large-scale model test for verifying the proposed concept without building a real-sized prototype to avoid miniaturization challenges such as high precision machining. Some major findings and contributions of this study are summarized next.

First, theoretical modeling of the tendon-gear mechanism was verified by the experiment using the large-scale prototype built based on the similarity analysis. Experimental results have shown good agreement between model-based estimation and measurement of the input–output relationships under the equivalent loading conditions, each of which was achieved from the real-sized model and the scaled-up prototype, respectively.

Second, the principle of elastic similarity was also validated by the aforementioned results. As stated earlier, the scaled-up prototype is kinematically equivalent but geometrically dissimilar to the real-sized model, because the geometric similarity was intentionally ignored in order for the enlarged prototype to be easily handled during the experiment. The fact that the elastic similitude between the different-sized models can be satisfied, even when their geometry is no longer similar, implies the increased flexibility and malleability of prototype design for the new laparoscopic tools, and thus the reduction of time and cost required for the prototype development.

Third, the feasibility of design concept of the hybrid instrument and the functionality of its output loss compensation were verified by the experiment using the developed prototype. The experimental results have also shown that the large-scale model test warranted by the elastic similarity analysis is not just useful for verification of the design concept, but also very powerful for evaluating the performance of the real-sized prototype.

However, the experimental results have also revealed some challenges to solve for more robust performance of the output loss compensation. It has been shown that the performance of current tension-based control is quite sensitive to the amount of friction, particularly in the full articulation of the joints. Therefore, more improvement needs to be made from the refinement of joint design and the friction modeling. First, the mechanical design of the joint needs to be modified to make the vertices of tendon smoother or more rounded, which are formed during the joint angulation, to reduce the large friction concentrated on them. Also, mathematical modeling of the friction between tendon and sheath, whose amount and direction are dependent on the configuration of the instrument, needs to be conducted and included in the tension-based estimation on the end-effector angle to overcome the tradeoff between accuracy and speed of the output loss compensation.

Acknowledgment

The authors would like to thank H. T. Kim at Movasu, Inc., for his help in elaborating the details of the patented design of the articulated instrument using tendon-gear mechanism.

References

[1] C. R. Tracy, J. D. Raman, J. A. Cadeddu, and A. Rane, "Laparoendoscopic single-site surgery in urology: Where have we been and where are we heading?" *Nature Clin. Pract. Urol.*, vol. 5, no. 10, pp. 561–568, 2008.

[2] J. R. Romanelli and D. B. Earle, "Single-port laparoscopic surgery: An overview," *Surg. Endoscopy*, vol. 23, no. 7, pp. 1419–1427, 2009.

[3] J. E. Humphrey and D. Canes, "Transumbilical laparoendoscopic single-site surgery in urology," *Int. J. Urol.*, vol. 19, no. 5, pp. 416–428, 2012.

[4] A. Faraz and S. Payandeh, "Automated devices," in *Engineering Approaches to Mechanical and Robotic Design for Minimally Invasive Surgery (MIS)*. Norwell, MA, USA: Kluwer, 2000, pp. 57–67.

[5] W.-J. Lee, "Single port laparoscopic surgery," *J. Korean Med. Assoc.*, vol. 53, no. 9, pp. 793–806, 2010.

[6] D. Canes, M. M. Desai, M. Aron, G.-P. Haber, R. K. Goel, R. J. Stein, J. H. Kaouk, and I. S. Gill, "Transumbilical single-port surgery: Evolution and current status," *Eur. Urol.*, vol. 54, no. 5, pp. 1020–1030, 2008.

[7] K. H. Rha, "The present and future of robotic surgery," *J. Korean Med. Assoc.*, vol. 51, no. 1, pp. 67–73, 2008.

[8] G. S. Choi, "Current status of robotic surgery: What is different from laparoscopic surgery?" *J. Korean Med. Assoc.*, vol. 55, no. 7, pp. 610–612, 2012.

[9] R. Autorino, J. H. Kaouk, J.-U. Stolzenburg, I. S. Gill, A. Mottrie, A. Tewari, and J. A. Cadeddu, "Current status and future directions of robotic single-site surgery: A systematic review," *Eur. Urol.*, vol. 63, no. 2, pp. 266–280, Feb. 2013.
[10] D. Nio, W. A. Bemelman, K. T. Boer, M. S. Dunker, D. J. Gouma, and T. M. Gulik, "Efficiency of manual versus robotical (Zeus) assisted laparoscopic surgery in the performance of standardized tasks," *Surg. Endoscopy*, vol. 16, no. 3, pp. 412–415, 2002.
[11] G. F. Dakin and M. Gagner, "Comparison of laparoscopic skills performance between standard instruments and two surgical robotic systems," *Surg. Endoscopy*, vol. 17, no. 4, pp. 574–579, 2003.
[12] H. Marcus, D. Nandi, A. Darzi, and G.-Z. Yang, "Surgical robotics through a keyhole: From today's translational barriers to tomorrow's disappearing robots," *IEEE Trans. Biomed. Eng.*, vol. 60, no. 3, pp. 674–681, Mar. 2013.
[13] P. Dario, M. C. Carrozza, M. Marcacci, S. D'Attanasio, B. Magnami, O. Tonet, and G. Megali, "A novel mechatronic tool for computer-assisted arthroscopy," *IEEE Trans. Inf. Technol. Biomed.*, vol. 4, no. 1, pp. 15–29, Mar. 2000.
[14] H. Yamashita, N. Hata, M. Hashizume, and T. Dohi, "Handheld laparoscopic forceps manipulator using multi-slider linkage mechanisms," in *Proc. Int. Conf. Med. Image Comput. Comput.-Assisted Intervention*, 2004, pp. 121–128.
[15] N. Zemiti, G. Morel, T. Ortmaier, and N. Bonnet, "Mechatronic design of a new robot for force control in minimally invasive surgery," *IEEE/ASME Trans. Mechatronics*, vol. 12, no. 2, pp. 143–153, Apr. 2007.
[16] A. H. Zahraee, J. K. Paik, J. Szewczyk, and G. Morel, "Toward the development of a hand-held surgical robot for laparoscopy," *IEEE/ASME Trans. Mechatronics*, vol. 15, no. 6, pp. 853–861, Dec. 2010.
[17] M. Piccigallo, F. Focacci, O. Tonet, G. Megali, C. Quaglia, and P. Dario, "Hand-held robotic instrument for dextrous laparoscopic interventions," *Int. J. Med. Robot. Comput.*, vol. 4, no. 4, pp. 331–338, 2008.
[18] V. Agrawal, W. J. Peine, and B. Yao, "Modeling of transmission characteristics across a cable-conduit system," *IEEE Trans. Robot.*, vol. 26, no. 5, pp. 914–924, Oct. 2010.
[19] F. Tendick, S. S. Sastry, R. S. Fearing, and M. Cohn, "Applications of micromechatronics in minimally invasive surgery," *IEEE/ASME Trans. Mechatronics*, vol. 3, no. 1, pp. 34–42, Mar. 1998.
[20] P. Puangmali, K. Althoefer, L. D. Seneviratne, D. Murphy, and P. Dasgupta, "State-of-the-art in force and tactile sensing for minimally invasive surgery," *IEEE Sens. J.*, vol. 8, no. 4, pp. 371–381, Apr. 2008.
[21] C. W. Jeong, "Tool for minimally invasive surgery," U.S. Patent US20110106146 A1, May 5, 2011.
[22] T. A. McMahon, "Scaling quadrupedal galloping: Frequencies, stresses, and joint angles," in *Scale Effects in Animal Locomotion*, T. J. Pedley, Ed. New York, NY, USA: Academic, 1977, pp. 143–151.
[23] R. A. Norberg, "Theory of growth geometry of plants and self-thinning of plant populations: Geometric similarity, elastic similarity, and different growth modes of plant parts," *Amer. Naturalist*, vol. 131, pp. 220–256, 1988.
[24] J. Koechling and H. Marc, "How fast can a legged robot run?" in *Robots and Biological Systems: Towards a New Bionics?* New York, NY, USA: Springer, 1993, pp. 239–269.
[25] R. M. Alexander, "Springs and control," in *Elastic Mechanisms in Animal Movement*. Cambridge, U.K.: Cambridge Univ. Press, 1988, pp. 110–128.
[26] R. M. Alexander, "Consequences of size differences" in *Principles of Animal Locomotion*. Princeton, NJ, USA: Princeton Univ. Press, 2013, pp. 53–67.
[27] B. Kübler, U. Seibold, and G. Hirzinger, "Development of actuated and sensor integrated forceps for minimally invasive robotic surgery," *Int. J. Med. Robot. Comput.*, vol. 1, no. 3, pp. 96–107, 2005.
[28] K.-Y. Kim, H.-S. Song, J.-W. Suh, and J.-J. Lee, "A novel surgical manipulator with workspace-conversion ability for telesurgery," *IEEE/ASME Trans. Mechatronics*, vol. 18, no. 1, pp. 200–211, Feb. 2013.
[29] D. B. Camarillo, C. F. Milne, C. R. Carlson, M. R. Zinn, and J. K. Salisbury, "Mechanics modeling of tendon-driven continuum manipulators," *IEEE Trans. Robot.*, vol. 24, no. 6, pp. 1262–1273, Dec. 2008.
[30] T. Kanno, D. Haraguchi, M. Yamamoto, K. Tadano, and K. Kawashima, "A forceps manipulator with flexible 4-DOF mechanism for laparoscopic surgery," *IEEE/ASME Trans. Mechatronics*, vol. 20, no. 3, pp. 1170–1178, Jun. 2015.

Yoon-Ho Kim received the B.S. degree in mechanical and aerospace engineering from Seoul National University, Seoul, Korea, in 2013.

From 2011 to 2013, he was a Research Assistant with the BioRobotics Laboratory at Seoul National University. His research interests include surgical robotics, human-robot interaction, and haptic interfaces. Since August 2013, he has been performing his military duty by working as a propulsion systems designer with the Naval and Special Ship Design Team at Daewoo Shipbuilding & Marine Engineering Co., Ltd. (DSME), Geoje, Korea.

Yong-Jai Park (M'14) received the B.S. and Ph.D. degrees in mechanical and aerospace engineering from Seoul National University, Seoul, Korea, in 2004 and 2013, respectively.

He was with Samsung Electronics in a managerial position from 2003 to 2005. He is currently an Assistant Professor of mechanical engineering and the Director of the Robot and Mechanism Laboratory, Sun Moon University, Asan, Korea. His research interests include robotic fish, biologically inspired robotics, surgical robotics, and novel mechanisms.

HyunKi In (S'09) received the B.S. and Ph.D. degrees in mechanical and aerospace engineering from Seoul National University, Seoul, Korea, in 2009 and 2015, respectively.

He is currently a postdoctoral fellow with the Biorobotics Laboratory at Seoul National University. His research interests include robotic mechanism, and rehabilitation and assistive robotics.

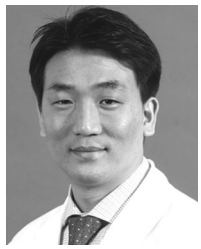

Chang Wook Jeong received the M.D., M.S., and Ph.D. degrees in medicine from Seoul National University, Seoul, Korea, in 2001, 2005, and 2011, respectively.

He had his internship and residency training in the Department of Urology, Seoul National University Hospital, Seoul, from 2001 to 2006, where he is currently an Associate Professor. He obtained clinical fellowships from the same hospital and Seoul National University Bundang Hospital in 2010 and 2011, respectively. He was an Assistant Professor in the Department of Urology, Seoul National University Bundang Hospital from 2011 to August 2013.

Kyu-Jin Cho (M'08) received the B.S and M.S. degrees from Seoul National University, Seoul, Korea, in 1998 and 2000, respectively, and the Ph.D. degree in mechanical engineering from the Massachusetts Institute of Technology in 2007.

He was a Postdoctoral Fellow with Harvard Microrobotics Laboratory until 2008. At present, he is an Associate Professor of mechanical and aerospace engineering and the Director of BioRobotics Laboratory at Seoul National University. His research interests include biologically inspired robotics, soft robotics, soft wearable devices, novel mechanisms using smart structures, and rehabilitation and assistive robotics. He has received the 2014 IEEE RAS Early Academic Career Award, 2014 ASME Compliant Mechanism Award, 2013 IROS Best Video Award, and 2013 KSPE Paik Am Award.